



Design Guidelines for Bioinspired Adaptive Foot for Stable Interaction With the Environment

Alok Ranjan , *Student Member, IEEE*, Franco Angelini , *Member, IEEE*,
Thrishantha Nanayakkara , *Senior Member, IEEE*, and Manolo Garabini , *Member, IEEE*

Abstract—Robotic exploration in natural environments requires adaptable, resilient, and stable interactions with uncertain terrains. Most state-of-the-art legged robots utilize flat or ball feet that lack adaptability and are prone to slip due to point contact with the ground. In this article, we present guidelines to design an adaptive foot that can interact with the terrain to achieve a stable configuration. The foot is inspired by goat hoof anatomy that incorporates roll and yaw rotations in the Fetlock and Pastern joints, respectively. To ensure adaptability with stability in physical interaction and to prevent the foot from collapsing, we provide a lower bound on each joint's stiffness. In addition, we also render an upper bound to conform to the high force exchange during interactions with the ground consisting of certain roughness. Based on these guidelines, we design the hoof and experimentally validate the theoretical results with a loading test setup in lab settings. We use four different friction materials with various triangular, rectangular, and semicircular extrusions to simulate common ground features. We observe that hooved pads require more load for the system to be unstable. Any anatomically inspired foot can be designed based on the guidelines proved analytically and experimentally in this article.

Index Terms—Biomimetic and bioinspired robotics, modeling and design, robotics.

I. INTRODUCTION

ANIMALS and humans effectively encounter structured and uneven terrains on a daily basis for their survival in this

Manuscript received 24 January 2023; revised 28 July 2023; accepted 21 September 2023. Recommended by Technical Editor G. Berselli and Senior Editor G. Berselli. This work was supported in part by the European Union's Horizon 2020 Research and Innovation Programme under Grant Agreement 101016970 (Natural Intelligence), in part by the Ministry of University and Research (MUR) as a part of the PON 2014-2021 "Research and Innovation" resources—Green/Innovation Action—DM MUR under Grant1062/2021, and in part by the Italian Ministry of Education and Research in the framework of the "FoReLab" (Future-oriented Research Lab) Project (Departments of Excellence). (*Corresponding author: Alok Ranjan.*)

Alok Ranjan, Franco Angelini, and Manolo Garabini are with the Centro di Ricerca "Enrico Piaggio", Dipartimento di Ingegneria dell'Informazione, Università di Pisa, 56122 Pisa, Italy (e-mail: alok.ranjan@phd.unipi.it; frncangelini@gmail.com; manolo.garabini@gmail.com).

Thrishantha Nanayakkara is with the Dyson School of Design Engineering, Imperial College London, SW7 2AZ London, U.K. (e-mail: t.nanayakkara@imperial.ac.uk).

This article has supplementary material provided by the authors and color versions of one or more figures available at <https://doi.org/10.1109/TMECH.2023.3326602>.

Digital Object Identifier 10.1109/TMECH.2023.3326602

world. Their exploration involves a complex and nonlinear dynamic interaction with the environment [1], [2], [3], [4], [5]. The locomotion task requires an integrated effort of the brain and the musculoskeletal system [6]. Legged locomotion facilitates them to select contact locations, adapt, and propel on the terrain. The bodily features that provide adaptation to the terrain are termed "morphological computations" [7], [8]. Humans and animals have evolved their morphological features to provide them with locomotion effectiveness and efficiency, which is very limited in their robotic counterparts. The anatomy of any animal's foot plays a crucial role in their locomotion as it has evolved with the interaction of their habitats through generations [9]. Therefore, it is significantly important to look into this aspect of locomotion and to come up with ideas that can help bridge the gap between animals and their robotic counterparts.

Major humanoids and quadruped robots to date are equipped with flat and ball feet, respectively. Most quadruped walkers (e.g., Spot [10], ANYmal [11]) use ball feet that make point contact with the ground. Traction on the contact is provided with a soft rubberized material, but despite this, foot slippage is a common problem. Robot foot is relatively less explored yet it is one of the most crucial components of the robot hardware. It directly makes contact with the terrain and is responsible for the physical interaction, gripping, and adaptation.

In our approach of providing robustness in stable foot-ground interactions, we present guidelines to design and test a bio-inspired adaptive foot. We take foot design inspirations from [13] that delve into the anatomy of a mountain goat foot and discuss the significant parameters of hoof design that provide the effectiveness of locomotion in highly uneven terrains. It also provides an important comparison between the goat's hoof and the ball foot through experimental validation. It reports that the work required for hoof slippage is three times that of the ball foot. The cloven foot has hooves that are pointed in the front and have a bulb shape on the rear. They are made of a hard keratin layer on the outside, and the sole is made of a rough soft keratinized epidermis material [14], [15]. The pointed hooves project forward into the soil to enhance stability, whereas soft sole provides excellent traction [16]. Utilizing hoof architecture seems beneficial because the impact force on the leg is not only absorbed through the footpad material but also by the foot features. Hooves provide the possibility to design a foot that is adaptable to ground features like rocks, slopes, and depressions. Moreover, hooves can engage with ground features that provide additional braking force. Morphological adaptations in both

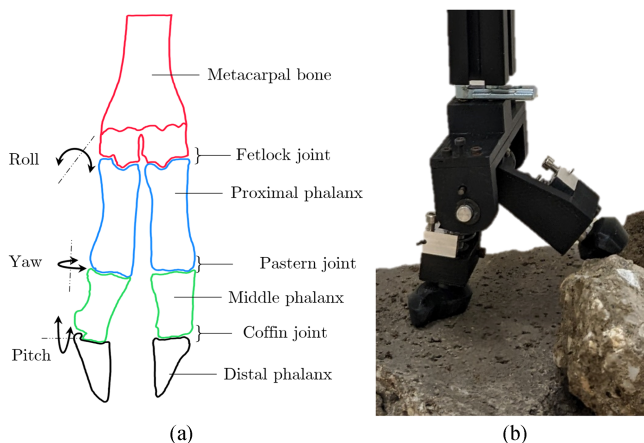


Fig. 1. (a) Line tracing from radiology of the pelvic limb of an adult small East African goat foot skeleton, adapted from [12]. (b) Bioinspired hoof-foot adapting and stabilizing on rocks.

kinematic features for passive gripping and dynamic features such as vibrations, friction, and restitution can lead to better slip reduction and stability that can be crucial for robots operating in natural environments [17].

The goat foot anatomy consists of three joints: fetlock, pastern, and coffin, which majorly provide roll, yaw, and pitch rotations, respectively [13]. Utilizing these features in a foot increases the complexity of the design, and then it is important to understand their beneficial contribution to the foot mechanism. There is limited literature present on goat hoof architecture, hence, we also use the literature presented on other cloven-hoofed Ruminants to provide a brief overview.

The skeleton and manus of ruminants are similar but vary in size, e.g., the manus of camel, bovine, goat, and sheep. Ruminants' hoof has two digits, and each consists of three phalanges—proximal, middle, and distal [18], [19]. An example of a goat's manus is shown in Fig. 1(a). The fetlock joints connect the proximal phalanges to the leg's metacarpal bone. These joints only flex and extend, which causes digit opening that can be controlled with a distal interdigital ligament capable of storing elastic energy. Fetlock joints provide roll motion to the digits. The pastern joints connect the proximal and middle phalanges. They are saddle joints due to the concavo-convex shape of the joint surfaces. They are biaxial joints that allow flexion and extension, and a limited range of lateral adjustments [18], [19], [20]. For simplification, we consider only the yaw rotation of the pastern joint as in [13] and [21]. The coffin joints connect the middle and distal phalanges. They are similar to the pastern joints [18], [19]. A horse's coffin joint allows movement in three planes with flexion and extension movements in the sagittal plane, lateromedial movements in the frontal plane, and rotation and sliding in the transverse plane. If a normal load is carried on a flat, level surface, the coffin joint's principal movement is flexion and extension [22], i.e., the pitch rotation. These three joints with flexion and extension tendons provide stability to the foot.

The contributions of this work are to provide guidelines that can help in designing adaptive feet that are similar to our design

presented in Fig. 1(b). With these guidelines, first, we identify the physical interaction of the adaptive foot with sloped terrain. Moreover, for a given maximum dynamic load we provide a lower bound on the roll and yaw joint's stiffness to ascertain the adaptation and stability of the foot mechanism. To sustain the high force exchange between foot and terrain due to ground roughness we also provide a higher bound on each joint's stiffness. This ensures that the maximum force generated during interaction should be lesser than that can be sustained by the foot structure. Furthermore, to validate the foot behavior we present a foot stability testing scheme in structured environments that bolsters the calculation of the stiffness bounds. Utilizing our guidelines of analytical and experimental design, feet with different anatomies can also be designed and tested.

II. STATE OF THE ART

In the past two decades, a wide range of humanoids have been developed that use flat feet. Some of them are ATLAS [23], HRP3 [24], HUBO [25], Nao [26], TORO [27], ASIMO [28], Valkyrie [29], Nadia [30], and Walkman [31]. To improve the rolling characteristics and increase the step length, some robots include a toe joint with passive stiffness in the flat foot design. For example, the foot of the humanoid M-Series [32], H6 [33], H7 [34], COMAN [35], and cCub [36] are designed for these characteristics. The humanoid robot LOLA [37] comprises a similar design with an active toe joint that allows the leg swing to be in a more extended configuration. WABIAN-2R [38] has two 1-DOF passive joints in its feet to enable it to bend its toes in steady walking. Some other bipedal robots utilize the elasticity of a carbon-fiber blade in the foot design. Bipedal robot Raptor [39] has a foot structure made of carbon/epoxy composite material that absorbs shock energy and reduces leg mass for low rotational inertia. BioBiped3 [40] utilizes the carbon fiber blade of a prosthetic foot to withstand a high ground reaction forces at impacts. Whereas, humanoid PETMAN [23] utilizes a compliant, carbon-fiber prosthetic foot that can fit inside a human footwear.

However, some other foot designs exist that actively and partially adapt to the environment [41], [42], [43] or have a flat foot with compliant elements within it [44], [45], [46]. For example, a rubber pad is utilized in [44], whereas [45] uses granular material enclosed in an airtight bag that allows the adaptation of the foot with controlled air pressure. In the biomimetic approach, a passive adaptive foot is designed in [47] that reflects the structure and movement of a human foot. A similar example of a bioinspired adaptive active foot with a compliant series-chain mechanism named SoftFoot is presented in [48]. Whereas, for a stable bipedal locomotion, a bioinspired robotic foot design that emulates the rotational motion of the human subtalar and oblique midtarsal joints, and compensates for the yaw moment in walking is presented in [49].

A bird-inspired biped BirdBot [50] has a leg with a digitigrade posture, in which the toe is the extension of the leg that becomes flat against the ground utilizing a clutch mechanism. The leg clutch and foot segment provide rapid spring engagement and adjustment of the center of pressure in direct response to

altered loading. Similarly, a bird-foot-inspired multisegmented foot design that resists slipping and sinking in natural terrains is presented in [51]. Their multisegmented foot design provides a large range of viable center of pressure that reduces foot sinking on soft substrates. Bipedal robots Tello [52], Cassie [53], and BRUCE [54] have a slimmer shaft-like foot that has similar to a line contact with the ground, and the actuation in roll direction is omitted.

Popular quadruped robots like Spot [10], ANYmal [11], Unitree Go1 [55], Mini Cheetah [56], and HyQ [57] are equipped with ball feet that have demonstrated their exceptional capabilities in structured and natural environments. They are prone to slip because the rounded shape of the foot makes point contact with the ground. Using a soft rubberized material and tread patterns on them provides some grip and adaptation to the environment. Soft materials also help in reducing the peak impact force on the legs and actuators. Adaptation through compliance and features in the foot is a key factor in better interacting with the terrain. The effect of different stiffness and damping properties on stability and the energetic economy of bipedal walking of ball-like feet is studied in [58]. Quadruped robots Oncilla [59] and Cheetah-cub [60] have a springy ankle joint with a short foot mounted to improve robustness, speed, and cost of transport.

Similar to the biomimetic foot SoftFoot, SoftFoot-Q [61] is designed for quadrupedal walkers, but it is passive in actuation. It also has a series of chains at the bottom of the mechanism that can adapt to different obstacle shapes. With that, the rotational ability about the pitch and yaw axes of the foot are two main adaptations. A bioinspired goat-hoof-based foot is coined in [13] that provides adaptability as well as requires three times more work to slip in comparison to a ball foot. The increased adaptability comes from the opening action of hooves.

Despite various developments of feet for humanoids and quadrupeds, there are not yet contributions to synthesize foot designs that provide a platform to analytically define the physical interaction of the foot with different terrain conditions. There are methods available to choose optimal stiffness and damping for impedance control in active systems [62], [63], but for passive joints, there is a need to find the lower and upper bounds on the foot stiffness behavior for a given dynamic loading condition to select springs that will provide both stability and resilience [64].

III. ANALYTICAL DESIGN GUIDELINES

Fig. 2 shows a brief representation of the workflow of the design guidelines that we propose. Here, we consider our design scheme as an example to show a step-by-step procedure for designing feet similar to our design.

1) First, we consider an animal for bioinspiration whose locomotion interests us based on the targeted environment. In our case, we are interested in the hoof architecture of *mountain goats* because of their agility in rocky environments. 2) We convert the skeletal architecture into the foot kinematics by specifying the anatomical joints. 3) We simplify the design by fusing the two parallel roll joints within the same axis. This reduces the number of design parameters in the theoretical analysis. We are

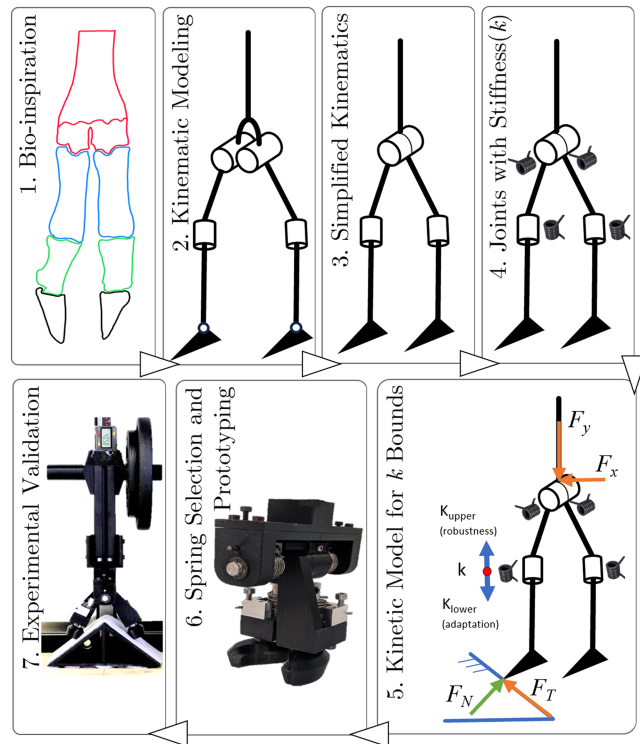


Fig. 2. Design process of a bioinspired adaptive foot.

interested in understanding the role of roll and yaw rotations as the pitch can also be accommodated about the knee and ankle joints. Introducing pitch stiffness on the distal phalanx can also result in a fragile hoof. Therefore, to simplify the design, we eliminate the pitch rotation considerations. 4) We add compliance in all the joints to integrate adaptability and resilience into the foot. 5) We write a physical interaction model to find lower and upper bounds on each joint's stiffness based on the foot design parameters and loading conditions during interactions. This will lead to a tradeoff between adaptability and stability. 6) The stiffness bounds help us to select springs for roll and yaw joints. We then proceed with the CAD modeling and prototyping. 7) We validate the performance of the foot by testing its behavior in the presence of different obstacle shapes and surface roughness.

For the physical interaction model at step 5), we consider planar force-stiffness models. We also consider that all the load on foot acts on a single digit for the worst-case scenario. To write the physical interaction model, we assume what follows:

1) *Rigid Body Motions*: In our physical interaction model, all bodies are considered rigid, including the terrain.

2) *Coulomb Friction*: As we are interested in the maximum loading condition, we have considered the Coulomb friction principle as a generator of the traction force. The Coulomb friction law for planar cases and the Coulomb friction cone are shown in Fig. 3. Therefore, the relation between the traction force F_T and the normal force F_N can be given as, $F_T = \mu F_N$, where μ is the coefficient of friction between the foot and the ground material [65], [66].

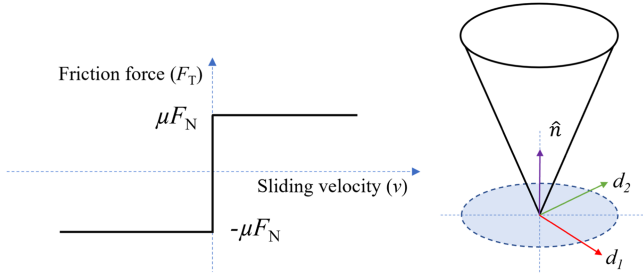


Fig. 3. Coulomb friction principle. In-plane(left) and friction cone (right) models.

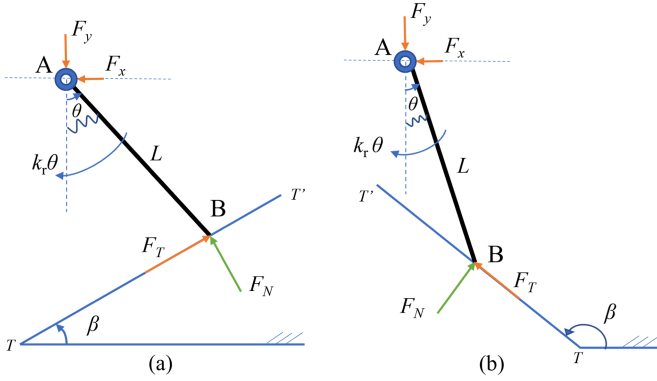


Fig. 4. Physical interaction model of hoof digit with the inclined terrain, where F_T is uphill. (a) $0^\circ < \beta < 90^\circ$. (b) $90^\circ < \beta < 180^\circ$.

In the following, we study the physical interaction of individual features focusing on foot stability and resilience.

A. Roll Stiffness Analysis: Lower Bound

Fig. 4 depicts the interaction between the digit AB of length L in contact with terrain $T-T'$ at point B . The digit has a revolute joint about point A (i.e., roll joint) and can have in-plane rotations. A torsional spring of lumped stiffness k_r is equipped at the roll joint that opposes the in-plane rotation of link AB . The loading on the foot at point A can be represented into horizontal and vertical components of magnitude F_x and F_y , respectively. When the digit makes contact with the terrain of β inclination, we consider that the reaction force on the digit results in a normal F_N and a traction force F_T at contact point B , which causes θ rotation of the digit from the downward global vertical axis.

For the roll case, the physical interaction between the digit and the terrain can be generalized in four piecewise cases. *Case 1*: $0^\circ < \beta < 90^\circ$, and traction force is in uphill direction [see Fig. 4(a)]; *Case 2*: $0^\circ < \beta < 90^\circ$, and traction force is in downhill direction; *Case 3*: $90^\circ < \beta < 180^\circ$, and traction force is in uphill direction [see Fig. 4(b)]; and *Case 4*: $90^\circ < \beta < 180^\circ$, and traction force is in downhill direction.

We start focusing on Case 1 [see Fig. 4(a)]. The goal is to determine the stiffness value for which the hoof digit is stable while interacting with the terrain. For this, we use the classical definition of a stable equilibrium point, i.e., an equilibrium point is defined as stable if the system state does not move indefinitely far from the equilibrium itself after a small perturbation [67].

To this end, we write the horizontal, vertical, and moment equilibrium equations, i.e.,

$$\Sigma H = 0 \rightarrow +ve$$

$$\mu F_N \cos(\beta) - F_N \sin(\beta) - F_x = 0 \quad (1)$$

$$\Sigma V = 0 \uparrow +ve$$

$$F_N \cos(\beta) + \mu F_N \sin(\beta) - F_y = 0 \quad (2)$$

$$\Sigma M_A = 0 \curvearrowright +$$

$$k_r \theta = F_N L (\mu \cos(\beta - \theta) - \sin(\beta - \theta)). \quad (3)$$

To ensure that the equilibrium point is stable, we set a lower bound k_{r1} for the stiffness through the following Proposition.

Proposition 1: Let us consider any equilibrium point $\theta \in [0, \pi/2]$, which satisfies (1)–(3) for a set of parameters F_N , F_y , F_x , L , β , and μ . If and only if the stiffness k_r is such that

$$k_r \geq k_{r1} \triangleq F_y L, \quad (4)$$

then any equilibrium point $\theta \in [0, \pi/2]$ is marginally stable.

Proof: We solve (2) for F_N and substitute it in (3), yielding

$$k_r \theta = F_y L \frac{\mu \cos(\beta - \theta) - \sin(\beta - \theta)}{\mu \sin(\beta) + \cos(\beta)}. \quad (5)$$

Then, we linearize (5) w.r.t. θ about a given equilibrium point, obtaining

$$\hat{k}_r = F_y L \frac{\mu \sin(\beta - \theta) + \cos(\beta - \theta)}{\mu \sin(\beta) + \cos(\beta)}. \quad (6)$$

Here, \hat{k}_r presents the minimum stiffness value such that the equilibrium is marginally stable.

However, we can further study the system to simplify the expression of \hat{k}_r . Taking \hat{k}_r from (6) and substituting it into (5), allows us to explicit the value of μ , which, after a few algebraic computations, can be written as

$$\mu = \frac{\sin(\beta - \theta) + \theta \cos(\beta - \theta)}{\cos(\beta - \theta) - \theta \sin(\beta - \theta)}. \quad (7)$$

Substituting (7) in (6) leads to

$$\hat{k}_r = F_y L \frac{S_{\beta-\theta}^2 + C_{\beta-\theta}^2 + \theta \{C_{\beta-\theta} S_{\beta-\theta} - C_{\beta-\theta} S_{\beta-\theta}\}}{\theta \{C_{\beta-\theta} S_{\beta-\theta} - S_{\beta-\theta} C_{\beta-\theta}\} + \{S_{\beta-\theta} S_{\beta-\theta} + C_{\beta-\theta} C_{\beta-\theta}\}} \quad (8)$$

where C_α and S_α indicate $\cos(\alpha)$ and $\sin(\alpha)$, respectively. Using the trigonometric identities, (8) can be written as

$$\hat{k}_r = F_y L \frac{1}{\cos(\theta) + \theta \sin(\theta)} \quad \theta \in [0, \pi/2]. \quad (9)$$

Using (9), we can prove the *if* and the *only if* parts of the proposition. Using the derivative test, it is possible to prove that the right-hand side of (9) has only one maximum point for $\theta = 0$, which leads to $\hat{k}_r = F_y L$. To prove the *if* part, we notice that (4) provides k_{r1} , which is the minimum stiffness value larger or equal than the maximum \hat{k}_r that leads to marginal stability for all $\theta \in [0, \pi/2]$ and for all values of μ and β . To prove the *only if* part we notice that the maximum value of the right member of (9), representing the largest value of \hat{k}_r leading to marginal stability, fulfills (4). \square

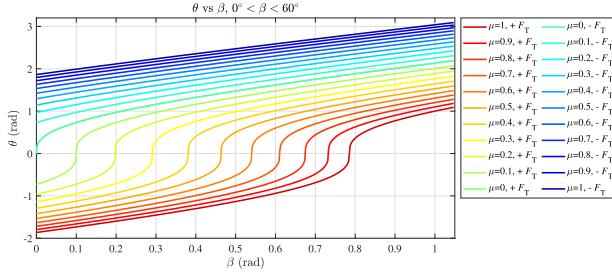


Fig. 5. Roll opening angle θ versus ground inclination β for $0^\circ < \beta < 60^\circ$, traction force is considered both uphill ($+F_T$) and downhill ($-F_T$).

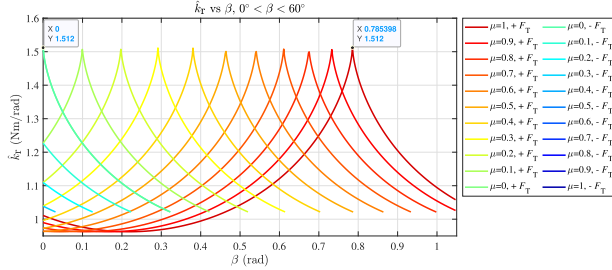


Fig. 6. Roll stiffness \hat{k}_r versus ground inclination β for $0^\circ < \beta < 60^\circ$, traction force is considered both uphill ($+F_T$) and downhill ($-F_T$).

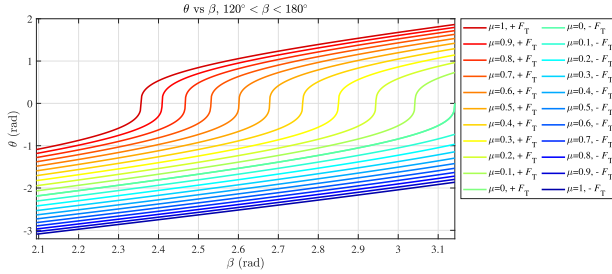


Fig. 7. Roll opening angle θ versus ground inclination β for $120^\circ < \beta < 180^\circ$, traction force is considered both uphill ($+F_T$) and downhill ($-F_T$).

Proposition 1 introduces a lower bound for the stiffness to achieve a marginally stable equilibrium in *Case 1*. Following similar steps, analogous conclusions can be drawn for all the other cases. We report the results here.

For *Case 1* and *Case 2*, Figs. 5 and 6 show the variation of the equilibrium θ w.r.t β , and the variation of the stiffness k_r at equilibrium θ w.r.t β , respectively. Similarly, for *Case 3* and *Case 4*, we plotted these variations together in Figs. 7 and 8, respectively. Fig. 5 shows that for $+F_T$, θ - β curves move rightward as the friction increases, whereas for $-F_T$, θ - β curves move leftward as the friction increases. This behavior is just the opposite in Fig. 7. Here, we are considering a vertical dynamic load $F_y = 20$ N on the foot that entirely transfers on a single digit. The length of the link $L = 75.6$ mm. Therefore, the maximum value of k_r for all μ and β at equilibrium θ is $k_{r1} = 1.512$ N·m/rad, which we can verify in Figs. 6 and 8.

B. Roll Stiffness Analysis: Upper Bound

The theoretical analysis in Section III-A proves that increasing the joint stiffness guarantees stability. Thus, a trivial approach

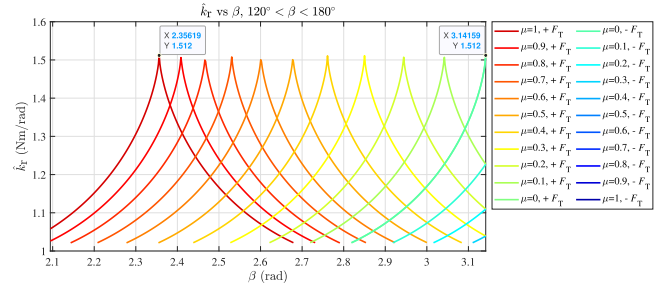


Fig. 8. Roll stiffness \hat{k}_r versus ground inclination β for $120^\circ < \beta < 180^\circ$, traction force is considered both uphill ($+F_T$) and downhill ($-F_T$).

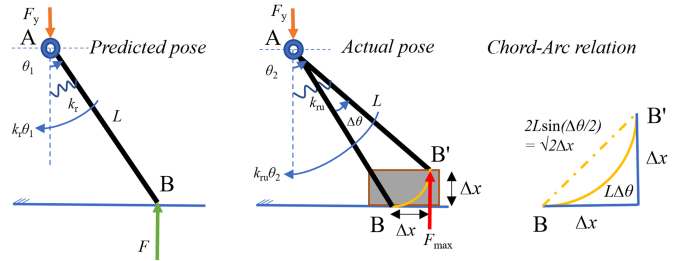


Fig. 9. Interaction of a digit with: Flat terrain (left), and rough terrain (mid). Displacement between predicted and actual contact pose is calculated with arc length (right).

would be to increase the stiffness as much as possible. However, there is a limit to the load the foot can bear. Let us consider that the maximum force that the foot structure can undergo without any failure is F_{\max} . This poses an upper bound k_{ru} to the stiffness. To compute it, we consider a case where a single digit undergoes an impact force F due to a collision with the ground. We can see in Fig. 9 that the collision occurs due to an obstacle of the order Δx ground roughness. If no obstacle is present and the pose is predicted correctly, the moment equilibrium can be written as

$$k_r \theta_1 = F L \sin(\theta_1). \quad (10)$$

In the presence of an obstacle, if the pose is not predicted correctly, and due to the collision, the rotation of the digit will be θ_2 instead of θ_1 , the relationship can be given as

$$\theta_2 = \theta_1 + \Delta\theta. \quad (11)$$

Substituting F_{\max} and (11) into (10) leads to

$$k_{ru} \theta_2 = F_{\max} L \sin(\theta_2), \quad \theta_2 \in [0, \pi/2]$$

or,

$$k_{ru} = F_{\max} L \frac{\sin(\theta_1 + \Delta\theta)}{\theta_1 + \Delta\theta}. \quad (12)$$

The value of $\Delta\theta$ in (12) is unknown. However, it is possible to compute it through the obstacle size Δx . To this end, consider the relationship between the arc and its chord depicted in Fig. 9. Given the length of the arc $L\Delta\theta$, it is possible to compute the chord length and equate it to the hypotenuse of an isosceles orthogonal triangle with catheti equal to Δx . This leads to

$$2L \sin(\Delta\theta/2) = \sqrt{2}\Delta x. \quad (13)$$

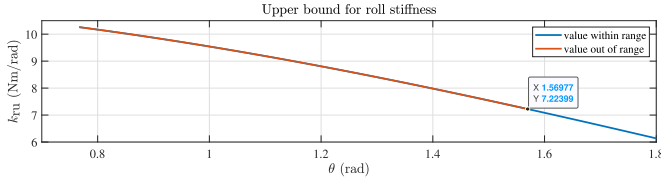


Fig. 10. Roll stiffness upper bound k_{ru} versus roll opening angle θ , the value of k_{ru} limits F_{max} for a maximum digit rotation of 90° .

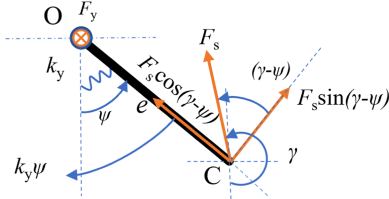


Fig. 11. Physical interaction model of the hoof with the terrain (top view).

Expliciting $\Delta\theta$ in (13) yields

$$\Delta\theta = 2 \arcsin(\Delta x / (\sqrt{2}L)). \quad (14)$$

Substituting (14) into (12) gives

$$k_{ru} = F_{max} L \frac{\sin(\theta_1 + 2 \arcsin(\Delta x / (\sqrt{2}L)))}{\theta_1 + 2 \arcsin(\Delta x / (\sqrt{2}L))}. \quad (15)$$

Equation (15) represents the maximum value of stiffness k_r that leads to a force exchange not greater than F_{max} in presence of ground roughness Δx .

Fig. 10 shows k_r w.r.t. θ for $F_{max} = 150$ N and $\Delta x = 40$ mm. The maximum value for the upper bound is $k_{ru} = 7.22$ N·m/rad.

C. Yaw Stiffness Analysis: Lower Bound

We consider the yaw stiffness model for the rotation of the hoof about its pivot. The physical interaction model is presented in Fig. 11. Here, the link OC of length e has a revolute joint about point O (i.e., yaw joint) and can have in-plane rotations. A torsional spring of lumped stiffness k_y is equipped at the yaw joint that opposes the in-plane rotation of link OC . The hoof contacts the terrain at point C , where the traction force F_s makes an angle $\gamma \in [\pi/2, 3\pi/2]$ with the global vertical that causes ψ rotation of the link. The traction force is the result of the normal reaction at C and the Coulomb friction between the ground and hoof $F_s = \mu F_N$.

The moment equilibrium equation can be written as

$$\Sigma M_O = 0 \quad \text{⊕} \quad (16)$$

$$k_y \psi = F_s \sin(\gamma - \psi)e = \mu F_N \sin(\gamma - \psi)e.$$

To ensure that the equilibrium point is stable, we set a lower bound k_{y1} for the stiffness through the following Proposition.

Proposition 2: Let us consider any equilibrium point $\psi \in [0, \pi/2]$, which satisfies (16) for a set of parameters F_N , F_s , e , γ , and μ . If and only if the stiffness k_y is such that

$$k_y \geq k_{y1} \triangleq \mu F_N e. \quad (17)$$

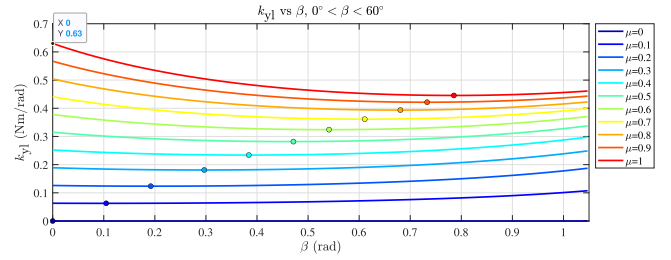


Fig. 12. Yaw stiffness k_{y1} versus ground inclination β for $0^\circ < \beta < 60^\circ$, uphill and downhill traction force both have same behavior. The round markers (o) show the minimum values for k_{y1} on the respective μ trends.

then any equilibrium point $\psi \in [0, \pi/2]$ is marginally stable.

Proof: Proceeding with the same steps adopted in Proposition 1, we differentiate (16) w.r.t. ψ , obtaining

$$\hat{k}_y = -\mu F_N \cos(\gamma - \psi)e. \quad (18)$$

\hat{k}_y represents the minimum stiffness value such that the equilibrium is marginally stable.

Given the fact that the stiffness should be positive, from trigonometric considerations, we can state that (18) has only one maximum point for $\psi = \gamma - \pi$, which leads to $\hat{k}_y = \mu F_N e$. To prove the *if* part we notice that (17) provides k_{y1} , which is the minimum stiffness value larger or equal than the maximum \hat{k}_y that leads to marginal stability for all $\psi \in [0, \pi/2]$. To prove the *only if* part, we notice that the maximum value of the right member of (18), representing the largest value of \hat{k}_y leading to marginal stability, fulfills (17). \square

There are four values for F_N based on the four cases mentioned in Section III-A. F_N from *Case 1* and *Case 3*, denotes that the foot is pushing on the terrain, whereas from *Case 2* and *Case 4*, it denotes that the foot is lifting up. We are interested in the value of F_N for *Case 1* and *Case 3*. We achieved the same results in both these cases. Based on the value of F_N from (2), we calculate stiffness for different β and μ values for a given link length $e = 31.5$ mm. The variation in the required stiffness for a stable equilibrium is shown in Fig. 12. The stiffness that stabilizes all considered interactions is $k_{y1} = 0.63$ N·m/rad, which can be verified from Fig. 12.

D. Yaw Stiffness Analysis: Upper Bound

Let us consider that the maximum force that the foot structure can undergo without any failure is F_{max} . This poses an upper bound k_{yu} to the stiffness. To compute it, we consider a physical interaction model similar to the one presented in Section III-B. Here, instead of the whole digit, only the hoof undergoes an impact force F . We can see in Fig. 13 that the collision occurs due to an obstacle of the order of Δh ground roughness. If no obstacle is present and the pose is predicted correctly, the moment of equilibrium can be written as

$$k_y \psi_1 = F e \sin(\psi_1). \quad (19)$$

In presence of an obstacle if the pose is not predicted correctly and due to the collision, the rotation of the digit is ψ_2 instead of

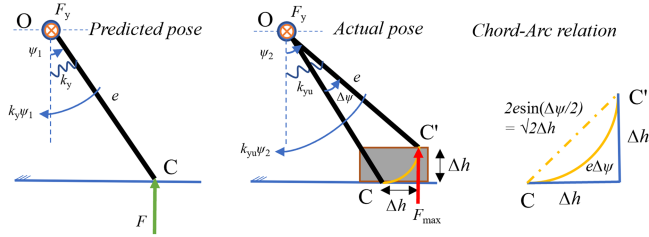


Fig. 13. Interaction (top view) of a hoof with: Flat terrain (left), and rough terrain (mid). Displacement between predicted and actual contact pose is calculated with arc length (right).

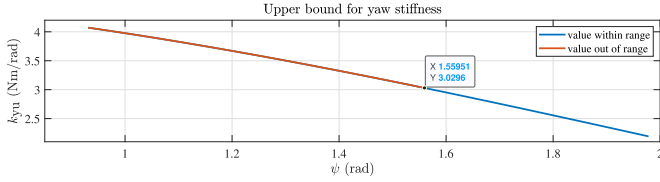


Fig. 14. Yaw stiffness upper bound k_{yu} versus yaw opening angle ψ , the value of k_{yu} limits F_{max} for a maximum hoof rotation of 90° .

ψ_1 , the relationship can be given as

$$\psi_2 = \psi_1 + \Delta\psi \quad (20)$$

Substituting F_{max} and (20) into (19) leads to

$$k_{yu}\psi_2 = F_{max}e \sin(\psi_2)$$

or,

$$k_{yu} = F_{max}e \frac{\sin(\psi_1 + \Delta\psi)}{\psi_1 + \Delta\psi}. \quad (21)$$

The value of $\Delta\psi$ in (21) is unknown. However, it is possible to compute it through the obstacle size Δh . To this end, consider the relationship between the arc and its chord, depicted in Fig. 13. Given the length of the arc $e\Delta\psi$, it is possible to compute the chord length and equate it to the hypotenuse of isosceles orthogonal triangle with catheti equal to Δh . This leads to

$$2e \sin(\Delta\psi/2) = \sqrt{2}\Delta h. \quad (22)$$

Evaluating $\Delta\psi$ in (22) yields

$$\Delta\psi = 2 \arcsin(\Delta h/(\sqrt{2}e)). \quad (23)$$

Substituting (23) into (21) gives

$$k_{yu} = F_{max}L \frac{\sin(\psi_1 + 2 \arcsin(\Delta h/(\sqrt{2}e)))}{\psi_1 + 2 \arcsin(\Delta h/(\sqrt{2}e))}. \quad (24)$$

Equation (24) represents the maximum value of stiffness k_y that leads to a force exchange not greater than F_{max} in presence of ground roughness Δh .

Fig. 14 shows k_{yu} w.r.t ψ for $F_{max} = 150$ N and $\Delta h = 20$ mm. The maximum value for the upper bound is $k_{yu} = 3.03$ N·m/rad.

IV. PROTOTYPE DESIGN

We implement the foot concept into a working prototype to deploy it for the experiments. We consider two types of foot pads: hemispherical and goat-hoof-anatomy-inspired, as shown

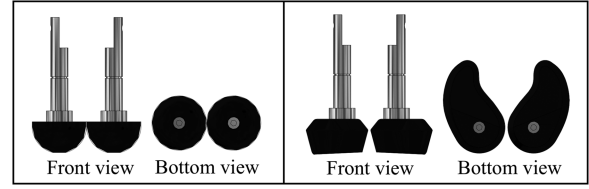


Fig. 15. Footpads: Hemispherical (left), and goat-hoof inspired (right).

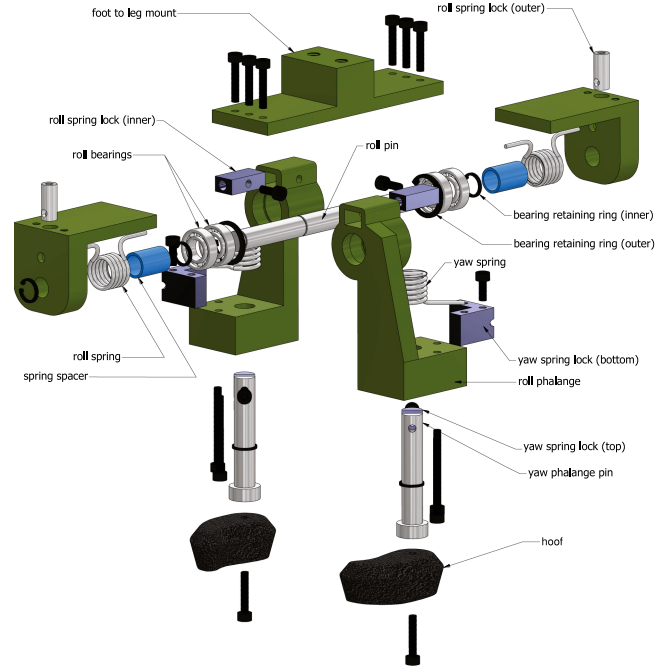


Fig. 16. Exploded view of the foot model.

TABLE I
FOOT DIMENSIONS

Parameter	Dimension
Digit length with hemispherical pad L	75.6mm
Hemispherical pad radius r	25mm
Digit length with hoof pad L_2	78.6mm
Hoof pad maximum radius e	31.5mm

in Fig. 15. For the roll case, the main design parameter is the digit length L from the roll axis to the farthest possible contact point. The radius of the hemispherical pad r or the thickness of hoof pad is included within L . For yaw rotation of hoof pad, the distance of the hoof tip from the yaw axis e is the main design parameter. We prepare a CAD model of the foot using these parameters. Further, we fabricate a physical prototype using mainly 3-D printed parts in ABS material. An exploded view of the hoof design is shown in Fig. 16. Corner and side views of the physical foot are shown in Fig. 17. It is also important to notice that during hoof-ground interactions, the distance between the contact point and roll axis is not always the same; however, to simplify the analytical analysis, we consider it constant. We choose the maximum value of L to ensure that the system is safe for all values. The foot dimensions are listed in Table I.

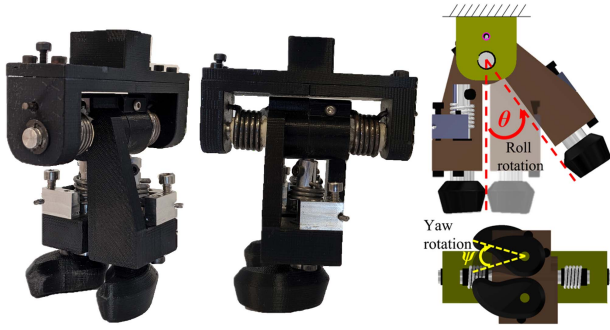


Fig. 17. Hoof-foot prototype printed in ABS with aluminum fixtures (left and mid). Examples of roll and yaw digit rotations (right).

TABLE II

JOINT STIFFNESS BOUNDS AND SELECTED SPRING STIFFNESS VALUES

	Analytical stiff. bounds	Eq.	Selected spring stiff.
Roll	lower	1.52Nm/rad (4)	1.55Nm/rad
	upper	7.22Nm/rad (15)	
Yaw	lower	0.63Nm/rad (17)	0.8Nm/rad
	upper	3.03Nm/rad (24)	

V. EXPERIMENTAL VALIDATION

We perform the experimental validation to assess the stability of the foot in the lab and in natural settings. We estimate the loading conditions that cause the foot to either slip gradually or make it suddenly unstable. The foot is fabricated with the possibility of changing the foot pads. We test both hemispherical and goat-hoof-inspired pads to assess the differences in both configurations. In Section III, we analytically provide a lower and an upper bound on roll and yaw stiffness to ensure stability and resilience. The computed values of analytical bounds for our setup are reported in Table II. To fulfill these theoretical bounds, we selected roll springs of stiffness $k_r = 1.55 \text{ N}\cdot\text{m}/\text{rad}$ and yaw springs of stiffness $k_y = 0.8 \text{ N}\cdot\text{m}/\text{rad}$.

A. Experimental Setup

We design tests to assess the stability behavior of roll and yaw spring stiffness in structured environments. A loading test setup is built with T-slotted aluminum profiles. One section of this profile is fixed on a flat table horizontally, and the other is fixed vertically at its center, which makes an arrangement similar to an upside-down T. A linear guide is mounted on the vertical profile coaxially. To test the stability of the roll spring, the foot is mounted on the slider such that the rolling axis of the foot is perpendicular to the translation axis of the linear guide, and the bottoms of both hooves are in a plane parallel to the table (*roll configuration*). Similarly, to test the stability of yaw springs, yaw phalanges are mounted on a test bracket separately (to eliminate roll dependence), keeping the yaw axes perpendicular to the translation axis of the linear guide and the tips of the hooves in a plane parallel to the table (*yaw configuration*). The tips of the hooves are kept open outwards so that when we load the tip, the moment opens the hoof instead of closing it.

In the analytical model, we consider the ground orientation from 0° to 180° . In the experimental tests, we aimed to validate the stability of the foot in these orientations. Therefore, we

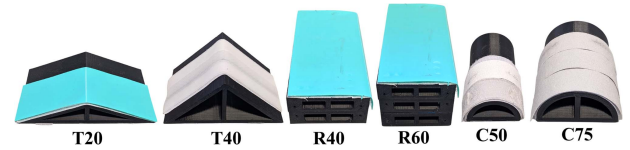


Fig. 18. Obstacles for ground features as mentioned in Table III.

TABLE III
OBSTACLE DIMENSIONS

Abb.	Profile description	Height
T20	Triangular cross-section with 20° base angles	30mm
T40	Triangular cross-section with 40° base angles	63mm
C50	Semicircular cross-section of 50mm diameter	25mm
C75	Semicircular cross-section of 75mm diameter	32.5mm
R40	Rectangular cross-section with 80mm width	40mm
R60	Rectangular cross-section with 80mm width	60mm

consider three types of profile extrusion for obstacles: triangular (T), rectangular (R), and semicircular (C). These profiles are considered because they can resemble most of the features in uneven ground and can provide all possible orientations of a ground plane. With semicircular obstacles, we can obtain a range of 0° to 180° orientations based on the contact location on the circular surface. Because the plane slope changes over the curvature, we consider two dimensions for the semicircular obstacles for different rates of change in the slope. With semicircular obstacles, the hooves do not contact it on the 0° and 90° planes. Hooves have a small gap in between that does not allow them to contact the 0° plane when the foot is mounted centered on the top, whereas the roll phalanges touch the obstacle before the hooves can reach the 90° planes. Therefore, we also consider a rectangular obstacle where the 0° and 90° planes are easily accessible. With triangular obstacles, we can obtain a specific orientation for the plane with a constant slope. For that, we selected two intermediate slopes for triangular obstacles. Thus, we test the stability of the foot in all orientations using these three types of obstacles. The obstacles are shown in Fig. 18. Their dimensions are mentioned in Table III.

To simulate different ground conditions, we placed four types of materials on top of the obstacles. The materials are selected to provide a coefficient of friction between 0 and 1 with 3-D printed ABS material of hoof. We want to study the contribution of morphological features of the hoof in slip reduction given an arbitrary surface friction coefficient. To determine the value of the sliding coefficient of friction, we perform inclined plane friction tests. We stick the ground materials on a plane and place a 3-D-printed ABS block on it. We increase the plane inclination until the block starts sliding. The expression $\mu = \tan(\omega)$ is used to calculate the coefficient of friction, where ω is the minimum angle for which the block slides. The obstacle materials, their thickness, and friction coefficient with 3-D printed ABS are listed in Table IV. M_1 and M_2 are relatively stiff materials, whereas M_3 and M_4 are soft and easily deformable ($M_3 > M_4$) against the loading.

B. Experimental Tests

To test the stability of roll springs, we mount the foot on the test setup in the roll configuration and load it against different

TABLE IV
MATERIAL DIMENSIONS AND CO-EFFICIENT OF FRICTION WITH
3-D PRINTED ABS

Abb.	Ground sheet materials	Thickness	μ
M ₁	Slippery polypropylene	0.5mm	0.22
M ₂	Dotted rubberized texture plastic	0.9mm	0.48
M ₃	Cork	1.96mm	0.6
M ₄	Aluminum abrasive anti slip material	1mm	1.04

TABLE V
LOADS (IN KG) THAT MAKE THE FOOT WITH HEMISPHERICAL AND
GOAT-HOOF PADS UNSTABLE WHEN PLACED ON DIFFERENT OBSTACLES
AND MATERIAL COMBINATIONS

Foot pad type	Obstacle	M1	M2	M3	M4
Hemispherical	T20	4.95	5.95	10.75	8.75
	T40	3.55	4.75	5.15	9.75
	C50	2.75	6.75	11.75	12.75
	C75	3.25	6.75	9.75	6.75
	R60	4.75	4.75	7.25	14.75
Goat-hoof	T20	4.95	16.75	>19.75	>19.75
	T40	3.75	4.75	13.75	10.25
	C50	5.75	7.75	>19.75	>19.75
	C75	5.35	7.75	>19.75	>19.75
	R60	3.55	4.75	13.75	14.75

obstacles. Similarly, to test the stability of yaw springs, we mount yaw phalanges on the test setup in the yaw configuration and load them against different obstacles. Triangular and semicircular obstacles are placed below the foot pads such that each foot pad touches the opposite faces of the obstacle about the axial plane of symmetry of the obstacle. The rectangular obstacle is placed below the foot pads such that one foot pad can slide on the horizontal face, while the other can slide on the vertical face of the obstacle.

In the theoretical analysis, we use the classical definition of a stable equilibrium point, where load variations on the foot are considered as perturbations. In our experiments, we slowly increase the load on the foot to observe hoof slippage. We make sure that hoof-obstacle contact is maintained and springs are active. If a large slip occurs due to an increment in the load, such that the obstacle comes in contact with parts of the foot other than the hooves (e.g., roll pin) the equilibrium is considered not to be stable anymore.

C. Experimental Results

The foot behavior against different obstacle profiles and materials is presented in this subsection. Abbreviations are used from Tables III and IV. The values in the Tables V and VI are loads that make the system just unstable. For the yaw case, the loads include the weight of the slider mechanism above the foot and applied dead weights. For the roll case, the weight of the foot is also added. The maximum available dead weight is 19 kg. The setup above the foot weighs approximately 0.5 kg, whereas the foot weighs 0.25 kg.

1) *Roll Stiffness Stability Test (Lower Bound)*: The experimental setup for this test is shown in Fig. 19. The values of the loads that collapse the foot or open it to the maximum possible limit gradually are shown in Table V. A comparison of how the load varies among different surface materials and types of foot

TABLE VI
LOADS (IN KG) TO PRODUCE MAXIMUM YAW DEFLECTION WITH HOOVED
PADS ON DIFFERENT OBSTACLES AND MATERIAL COMBINATIONS

Obstacle	M1	M2	M3	M4
T20	7.5	13.5	15.5*	>19.5*
T40	3.1	3.4	12.5	19.5 [†]
C50	5.1	17.5	13.5 [†]	17.5 [†]
C75	12.5	15.5	>19.5*	>19.5*
R60	9.5	10.5 [‡]	13.5 [†]	13.5 [†]

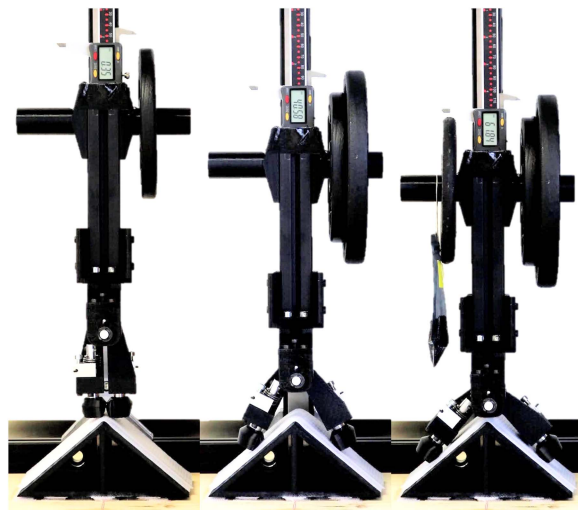


Fig. 19. Foot loaded for roll stiffness test on the linear guide setup.

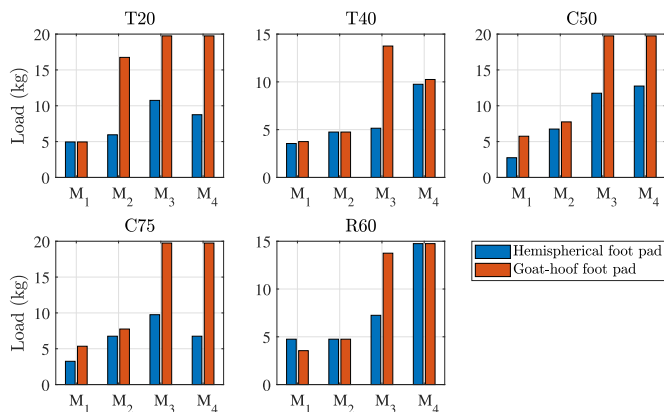


Fig. 20. Loads for instability when the foot is loaded in roll configuration on different obstacles and material combinations.

pads is shown in Fig. 20. For more details on the conducted experiments, please refer to the video attachment.

2) *Roll Stiffness Stability Test (Upper Bound)*: For this test, we use the rectangular obstacle R40 as the ground feature with material M₁. The load that opens the foot to the limit when the foot pad touches the ground is 6.75 kg in the hemispherical pad case and 8.75 kg in the hoof pad case. It is less than the permissible limit of 150 N (≈ 15.29 kg), and the maximum load

* Hooves start sinking into the material, as we increase the load there is no adaptation of the hoof to the obstacle.

[†] The material damages at this load and the hooves adapt to the shape.

[‡] The material is removed from the Velcro used to keep it in place.

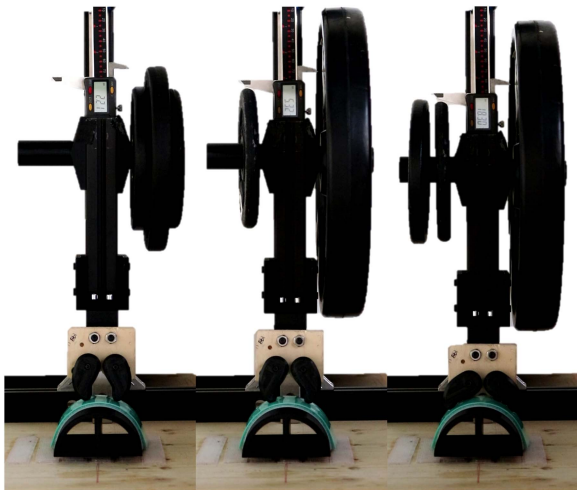


Fig. 21. Hooves loaded for yaw stiffness test on the linear guide setup.

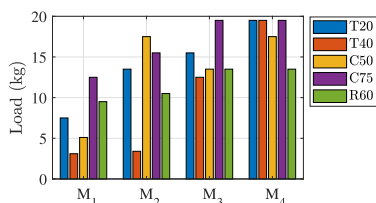


Fig. 22. Loads for instability when hooves are loaded in yaw configuration on different obstacles and material combinations.

the foot was able to hold during experiments, i.e., 19.75 kg. Therefore, the foot will be safe because of the adaptation of the foot happens at a much lower load.

3) *Yaw Stiffness Stability Test (Lower Bound)*: In the yaw case, observations are made to find the maximum load that opens hoof's yaw phalange digits to the maximum available deflection based on the obstacle profile. Because if the phalanges adapt to the obstacle shape, they cannot move anymore. Then the foot will see a rigid collision, which is not preferred. It can also be seen in Fig. 21. The values of the loads to achieve the maximum possible deflection are shown in Table VI. A comparison of how the load varies among different surface materials is shown in Fig. 22.

4) *Yaw Stiffness Stability Test (Upper Bound)*: We use the rectangular obstacle R40 as the ground feature in this test. Though the maximum possible vertical translation of the system is 20 mm, a 40 mm obstacle is used to give space for the other hoof to move. The load that opens the hoof pad is 12.5 kg. It is less than the permissible limit of 150 N (≈ 15.29 kg) and the maximum load the foot was able to take during experiments, i.e., 19.5 kg. Therefore, the foot will be safe because the adaptation of the hoof happens at a much lower load.

D. Experiments in Natural Settings

We test the foot in natural settings to show the qualitative behavior of foot adaptation to different obstacles that can be present in nature. For that, we mount the foot on one side of a bar



Fig. 23. Hoof-foot adapting and stabilizing on different obstacles in natural settings.

and place payloads on the other side of the bar. We keep the bar vertical so that all the payloads transfer to the foot. We applied loads within the 1–5 kg range. We also pushed the foot with our hands on multiple natural obstacles like wood, brick, and stones. We observed that the foot was able to conform to obstacles and provided stability in those scenarios. A few examples are presented in Fig. 23.

VI. DISCUSSIONS

During the experimental validation, we find that the minimum load to make the foot unstable (among all obstacles) for the roll stiffness test is 2.75 kg. For the yaw stiffness test, the minimum load to adapt the hooves to the obstacle profile is 3.1 kg. Because the system consists of two roll and two yaw springs, and both pairs are active during the aforementioned minimum value tests, the load-carrying capacity for one spring is half, that is, 1.375 kg for roll and 1.55 kg for yaw stiffness. We consider a dynamic load of $F_y = 20$ N (≈ 2.04 kg) during our analytical stiffness design for both springs, which we assume to be approximately three times the static load. Therefore, the static load is ≈ 0.7 kg. If we compare the worst-case scenarios with the static loading condition, the foot will not collapse during the operation. Approximately twice the static loading can be accommodated without foot collapse. However, if we try to fulfill the dynamic loading demand, in some cases, the foot collapses. The main reason for this is the choice of our springs. The stiffness values of the selected springs are very close to the theoretical lower bound. We choose them to keep the foot adaptable and not to make it stiff to disturbances. This problem can be solved by selecting slightly stiffer springs. For roll stiffness, we also observed that using hooved pads instead of hemispherical pads minimized this collapse for triangular obstacles and eliminated it for semicircular obstacles. This is mainly because hemispherical pads have a single-point contact that can convert into a contact patch based on the obstacle material. However, hooved pads either contact multiple points, or for soft obstacle materials, the entire edge can be in contact, which provides additional traction.

In addition, we observe that by increasing the contact friction with the ground, the foot generally requires more load to be unstable for all choices of obstacles and foot pads. Therefore, the foot should remain stable with higher contact friction conditions.

During roll stiffness tests, we observe that as the slope of the triangular obstacle increases, the foot remains stable for a lesser

force. Furthermore, as the radius of the semicircular obstacle increases, the foot remains stable for a higher force. When comparing the stability behavior between the hemispherical and hooved pads, we observe that generally, hooved pads can remain stable for higher loads. During the yaw stiffness test, we observe that as the slope of the triangular obstacle increases, it requires less force to open the hooves.

We also test the foot in natural conditions by placing it on a bar and loading it with payloads or a force applied by hands. In these experiments, we observe that the foot can stabilize itself on different natural obstacles.

During our experiments, different ground obstacles and contact friction with ground materials exhibit different modes of stability. With the slippery polypropylene sheet M_1 , we observe that the stability is mainly achieved with the stiffness of the roll or yaw springs in the respective cases. However, with the high-friction anti-slip material M_4 , the contact force is dominant, and the interaction is rather rigid because the digit is not able to slip and adjust to the obstacle's shape. If we increase the loading, eventually the contact breaks and the system becomes unstable, which causes foot collapse. This is because, at loads higher than the maximum dynamic loading, the springs are not able to hold the load. Therefore, with less load, the interaction is rigid, and with higher loads, it becomes unstable in a high-friction material condition.

Moreover, as the foot is mounted on a linear guide, for triangular and semicircular obstacles, it is assumed that both digits open simultaneously and equally to encounter the applied load. In this test setup, testing only one digit is not possible because allowing the digit to open about the roll axis requires horizontal and vertical displacement of the roll axis about the contact point in the no-slip condition. If we place the system on a linear guide, it only allows the vertical displacement of the roll axis. Therefore, in this constrained situation, only a symmetric opening of the foot is possible to test. In some cases, due to the high friction between the foot and ground, we provide an initial opening to the foot to ease adaptation. For the rectangular obstacle, instead of allowing both digits to slip on the flat surface, digits are pressed against the edge of the rectangle. This allows one digit to slip on the horizontal surface and the other on the vertical surface. Therefore, both springs are involved in triangular and semicircular obstacles. However, for the rectangular obstacle, only one spring is involved.

During our experiments, we observe that the requirement of stiffness is small if the foot should be opened to adapt. However, the foot collapses if the stiffness remains small while opening the digit to its limit. As the angular rotation of the spring increases, the torque provided by the spring increases but on the other hand, the eccentricity of the load also increases, and hence the loading torque. To prevent the foot from collapsing, the spring torque should always be greater than the loading torque on the digit. Therefore, to prevent collapse, we will require springs with a nonlinear stiffness that provide much higher torque on higher deflections.

Another observation is that when the foot is near zero roll condition, the tendency to open the foot is less as the eccentricity of the load from the roll axis is less. As the foot opens,

the eccentricity increases and that makes the foot open more easily. This behavior brings the possibility for improving the mechanism by reverting the tendency of foot opening, which can be explored in the next design.

VII. CONCLUSION

In this article, we presented a proof-of-concept robotic foot based on goat-hoof anatomy and discussed guidelines for designing feet that can make stable and resilient interactions with the environment. For soft foot-terrain interaction, it is crucial to incorporate adaptation properties into the foot design. Selecting joint stiffness is not a trivial task. We presented an analytical model design to find a range for the stiffness of the fetlock and pastern joints. Theoretical predictions have been experimentally validated confirming the expected behavior within the required parameters range (e.g., load and terrain shape). The fetlock joints can withstand a minimum load of 3.75 kg for $\mu = 0.22$ and 10.25 kg for the $\mu = 1.04$ at a terrain inclination of 40° . The pastern joints can withstand a minimum load of 3.1 kg for $\mu = 0.22$ at a slope of 40° , and at least 13.5 kg for the $\mu = 1.04$ if the hooves directly bump into a flat surface obstacle. This result enables to manage the adaptability and stability tradeoff in designing feet for legged robots.

In future work, foot design can be advanced with the inclusion of a coffin joint. In addition, the phalanx dimension and design will be optimized considering the robot parameters and obstacle sizes. The springs with a nonlinear stiffness behavior could increase compliance and adaptability at low deflections and prevent the foot from collapsing at large ones. We envision that such articulated foot designs will replace conventional ball foot designs in future legged robots.

REFERENCES

- [1] R. Full et al., "Templates and anchors: Neuromechanical hypotheses of legged locomotion on land," *J. Exp. Biol.*, vol. 202, no. 23, pp. 3325–3332, Dec. 1999.
- [2] L. Wang et al., "Design and dynamic locomotion control of quadruped robot with perception-less terrain adaptation," *Cyborg Bionic Syst.*, vol. 2022, 2022, Art. no. 9816495.
- [3] H.-W. Huang et al., "Mobile robotic platform for contactless vital sign monitoring," *Cyborg Bionic Syst.*, vol. 2022, 2022, Art. no. 9780497.
- [4] C. Huang et al., "Multimodal locomotion and cargo transportation of magnetically actuated quadruped soft microrobots," *Cyborg Bionic Syst.*, vol. 2022, 2022, Art. no. 0004.
- [5] A. Torres-Pardo et al., "Legged locomotion over irregular terrains: State of the art of human and robot performance," *Bioinspiration Biomimetics*, vol. 17, no. 6, 2022, Art. no. 061002.
- [6] A. C. Murphy et al., "Structure, function, and control of the human musculoskeletal network," *PLOS Biol.*, vol. 16, pp. 1–27, Jan. 2018.
- [7] V. C. Müller et al., "What is morphological computation? On how the body contributes to cognition and control," *Artif. Life*, vol. 23, no. 1, pp. 1–24, Feb. 2017.
- [8] K. Ghazi-Zahedi et al., "Evaluating morphological computation in muscle and dc-motor driven models of hopping movements," *Front. Robot. AI*, vol. 3, 2016, Art. no. 42. [Online]. Available: <https://www.frontiersin.org/articles/10.3389/frobt.2016.00042/full>
- [9] T. Kubo et al., "Transitions between foot postures are associated with elevated rates of body size evolution in mammals," *Proc. Nat. Acad. Sci. USA*, vol. 116, no. 7, pp. 2618–2623, 2019.
- [10] E. Guizzo, "By leaps and bounds: An exclusive look at how boston dynamics is redefining robot agility," *IEEE Spectr.*, vol. 56, no. 12, pp. 34–39, Dec. 2019.

- [11] M. Hutter et al., "ANYmal - A highly mobile and dynamic quadrupedal robot," in *Proc. IEEE/RSJ Int. Conf. Intell. Robots Syst.*, 2016, pp. 38–44.
- [12] M. Makungu, "Gross osteology and radiology of the pelvic limb of the adult small East African Goat," *Anatomia Histologia Embryologia*, vol. 48, pp. 234–243, May 2019.
- [13] S. A. Abad, N. Sornkarn, and T. Nanayakkara, "The role of morphological computation of the goat hoof in slip reduction," in *Proc. IEEE Int. Conf. Intell. Robots Syst.*, 2016, pp. 5599–5605.
- [14] D. H. Chadwick, *A Beast the Color of Winter: The Mountain Goat Observed*. Lincoln, Nebraska: Univ. Nebraska Press, 2002.
- [15] H. Kui et al., "The passive contact stability of blue sheep hoof based on structure, mechanical properties, and surface morphology," *Front. Bioeng. Biotechnol.*, vol. 8, 2020, Art. no. 363. [Online]. Available: <https://www.frontiersin.org/articles/10.3389/fbioe.2020.00363/full>
- [16] Q. Zhang et al., "Design and kinematics analysis of a bionic mechanical goat hoof," *Appl. Mech. Mat.*, vol. 461, pp. 191–200, Feb. 2014.
- [17] F. Angelini et al., "Robotic monitoring of habitats: The natural intelligence approach," *IEEE Access*, vol. 11, pp. 72575–72591, 2023.
- [18] Q. Zhang et al., "Terrain adaptability mechanism of large Ruminants' feet on the kinematics view," *Appl. Bionics Biomech.*, vol. 2015, pp. 1–9, 2015.
- [19] Q. Zhang et al., "Investigation of feet functions of large Ruminants with a decoupled model of equivalent mechanism," *Biol. Open*, vol. 6, no. 4, pp. 407–414, Apr. 2017.
- [20] H. E. König et al., *Vet. Anatomy of Domestic Mammals: Textbook and Colour Atlas*. Stuttgart, Germany: Schattauer, 2009.
- [21] S.-A. Abad, N. Herzog, S. M. H. Sadati, and T. Nanayakkara, "Significance of the compliance of the joints on the dynamic slip resistance of a bioinspired hoof," *IEEE Trans. Robot.*, vol. 35, no. 6, pp. 1450–1463, Dec. 2019.
- [22] S. J. Dyson, *Chapter 33—The Distal Phalanx and Distal Interphalangeal Joint*. 2nd ed., M. W. Ross et al., Eds. Philadelphia, PA, USA: W. B. Saunders, 2011.
- [23] G. Nelson et al., "The PETMAN and Atlas Robots at Boston dynamics," in *Humanoid Robotics: A Reference*. Dordrecht, Netherlands: Springer, 2017, pp. 1–18.
- [24] K. Kaneko, K. Harada, F. Kanehiro, G. Miyamori, and K. Akachi, "Humanoid robot HRP-3," in *Proc. IEEE/RSJ Int. Conf. Intell. Robots Syst.*, 2008, pp. 2471–2478.
- [25] I. W. Park, J.-Y. Kim, J. Lee, and J.-H. Oh, "Mechanical design of humanoid robot platform KHR-3 (KAIST Humanoid Robot - 3: HUBO)," in *Proc. IEEE-RAS 5th Int. Conf. Humanoid Robots*, 2005, pp. 321–326.
- [26] D. Gouaillier et al., "Mechatronic design of NAO humanoid," in *Proc. IEEE Int. Conf. Robot. Autom.*, 2009, pp. 769–774.
- [27] J. Engelsberger et al., "Overview of the torque-controlled humanoid robot TORO," in *Proc. IEEE-RAS Int. Conf. Humanoid Robots*, 2015, pp. 916–923.
- [28] M. Hirose et al., "Honda humanoid robots development," *Philos. Trans. Roy. Soc. A: Math. Phys. Eng. Sci.*, vol. 365, pp. 11–19, Nov. 2006.
- [29] N. A. Radford et al., "Valkyrie: NASA's first bipedal humanoid robot," *J. Field Robot.*, vol. 32, pp. 397–419, May 2015.
- [30] *Nadia humanoid – IHMC robotics lab.*, Accessed: Jul. 28, 2023. [Online]. Available: <http://robots.ihmc.us/nadia>
- [31] F. Negrello et al., "WALK-MAN humanoid lower body design optimization for enhanced physical performance," in *Proc. IEEE Int. Conf. Robot. Autom.*, 2016, pp. 1817–1824.
- [32] D. Lukac, T. Siedel, and C. Benckendorff, "Designing the test feet of the humanoid robot m-series," in *Proc. 22nd Int. Symp. Inf. Commun. Autom. Technol.*, 2009, pp. 1–6.
- [33] K. Nishiwaki, S. Kagami, Y. Kuniyoshi, M. Inaba, and H. Inoue, "Toe joints that enhance bipedal and fullbody motion of humanoid robots," in *Proc. IEEE Int. Conf. Robot. Autom.*, 2002, pp. 3105–3110.
- [34] K. Nishiwaki et al., "The experimental humanoid robot H7: A research platform for autonomous behaviour," *Philos. Trans. Roy. Soc. A: Math. Phys. Eng. Sci.*, vol. 365, pp. 79–107, Nov. 2006.
- [35] P. Kormushev, B. Ugurlu, S. Calinon, N. G. Tsagarakis, and D. G. Caldwell, "Bipedal walking energy minimization by reinforcement learning with evolving policy parameterization," in *Proc. IEEE/RSJ Int. Conf. Intell. Robots Syst.*, 2011, pp. 318–324.
- [36] N. G. Tsagarakis, Zhibin Li, J. Saglia, and D. G. Caldwell, "The design of the lower body of the compliant humanoid robot "cCub"," in *Proc. IEEE Int. Conf. Robot. Autom.*, 2011, pp. 2035–2040.
- [37] T. Buschmann et al., "Humanoid robot lola: Design and walking control," *J. Physiol.-Paris*, vol. 103, no. 3, pp. 141–148, 2009.
- [38] Y. Ogura et al., "Human-like walking with knee stretched, heel-contact and toe-off motion by a humanoid robot," in *Proc. IEEE/RSJ Int. Conf. Intell. Robots Syst.*, 2006, pp. 3976–3981.
- [39] J. Park, J. Lee, J. Lee, K. -S. Kim, and S. Kim, "Raptor: Fast bipedal running and active tail stabilization," in *Proc. 11th Int. Conf. Ubiquitous Robots Ambient Intell.*, 2014, pp. 215–215.
- [40] M. A. Sharbafi et al., "A new biarticular actuator design facilitates control of leg function in biobiped3," *Bioinspiration Biomimetics*, vol. 11, no. 4, Jul. 2016, Art. no. 046003.
- [41] S. Davis and D. G. Caldwell, "The design of an anthropomorphic dexterous humanoid foot," in *Proc. IEEE/RSJ Int. Conf. Intell. Robots Syst.*, 2010, pp. 2200–2205.
- [42] H.-J. Kang et al., "Realization of biped walking on uneven terrain by new foot mechanism capable of detecting ground surface," in *Proc. IEEE Int. Conf. Robot. Autom.*, 2010, pp. 5167–5172.
- [43] D. Kuehn et al., "Active spine and feet with increased sensing capabilities for walking robots," in *Proc. Int. Symp. Artif. Intell. Robot. Autom. Space*, 2012, pp. 4–6.
- [44] J. Li, Q. Huang, W. Zhang, Z. Yu, and K. Li, "Flexible foot design for a humanoid robot," in *Proc. IEEE Int. Conf. Autom. Logistics*, 2008, pp. 1414–1419.
- [45] A. Najmuddin, Y. Fukuoka, and S. Ochiai, "Experimental development of stiffness adjustable foot sole for use by bipedal robots walking on uneven terrain," in *Proc. IEEE/SICE Int. Symp. Syst. Integration*, 2012, pp. 248–253.
- [46] N. G. Tsagarakis, Z. Li, J. Saglia, and D. G. Caldwell, "The design of the lower body of the compliant humanoid robot "cCub"," in *Proc. IEEE Int. Conf. Robot. Autom.*, 2011, pp. 2035–2040.
- [47] J.-T. Seo and B.-J. Yi, "Modeling and analysis of a biomimetic foot mechanism," in *Proc. IEEE/RSJ Int. Conf. Intell. Robots Syst.*, 2009, pp. 1472–1477.
- [48] C. Piazza et al., "Toward an adaptive foot for natural walking," in *Proc. IEEE-RAS Int. Conf. Humanoid Robots*, 2016, pp. 1204–1210.
- [49] T.-Y. Chen et al., "Bevel-gear mechanical foot: A bioinspired robotic foot compensating yaw moment of bipedal walking," *Adv. Robot.*, vol. 36, no. 13, pp. 631–640, 2022.
- [50] A. Badri-Spröwitz et al., "Birdbot achieves energy-efficient gait with minimal control using avian-inspired leg clutching," *Sci. Robot.*, vol. 7, no. 64, 2022, Art. no. eabg4055.
- [51] A. Chatterjee et al., "Multi-segmented adaptive feet for versatile legged locomotion in natural terrain," in *Proc. IEEE Int. Conf. Robot. Automat.*, London, U.K., 2023, pp. 1162–1169, doi: [10.1109/ICRA48891.2023.10161515](https://doi.org/10.1109/ICRA48891.2023.10161515).
- [52] Y. Sim and J. Ramos, "Tello leg: The study of design principles and metrics for dynamic humanoid robots," *IEEE Robot. Autom. Lett.*, vol. 7, no. 4, pp. 9318–9325, Oct. 2022.
- [53] Y. Gong et al., "Feedback control of a Cassie bipedal robot: Walking, standing, and riding a segway," in *Proc. Amer. Control Conf.*, 2019, pp. 4559–4566.
- [54] Y. Liu, J. Shen, J. Zhang, X. Zhang, T. Zhu, and D. Hong, "Design and control of a miniature bipedal robot with proprioceptive actuation for dynamic behaviors," in *Proc. Int. Conf. Robot. Autom.*, 2022, pp. 8547–8553.
- [55] *Unitreebotics.*, Accessed: Jul. 28, 2023. [Online]. Available: <https://shop.unitree.com/>
- [56] B. Katz, J. D. Carlo, and S. Kim, "Mini Cheetah: A platform for pushing the limits of dynamic quadruped control," in *Proc. Int. Conf. Robot. Autom.*, 2019, pp. 6295–6301.
- [57] C. Semini et al., "Design of the Hydraulically Actuated, Torque-Controlled Quadruped Robot HyQ," *IEEE/ASME Trans. Mechatronics*, vol. 22, no. 2, pp. 635–646, Apr. 2017, doi: [10.1109/TMECH.2016.2616284](https://doi.org/10.1109/TMECH.2016.2616284).
- [58] E. Schumann, N. Smit-Anseeuw, P. Zaytsev, R. Gleason, K. A. Shorter, and C. D. Remy, "Effects of foot stiffness and damping on walking robot performance," in *Proc. Int. Conf. Robot. Autom.*, 2019, pp. 3698–3704.
- [59] A. T. Spröwitz et al., "Oncilla robot: A versatile open-source quadruped research robot with compliant pantograph legs," *Front. Robot. AI*, vol. 5, 2018, Art. no. 67. [Online]. Available: <https://www.frontiersin.org/articles/10.3389/frobot.2018.00067/full>
- [60] A. Spröwitz et al., "Towards dynamic trot gait locomotion: Design, control, and experiments with cheetah-cub, a compliant quadruped robot," *Int. J. Robot. Res.*, vol. 32, no. 8, pp. 932–950, 2013.
- [61] M. G. Catalano et al., "Adaptive feet for quadrupedal walkers," *IEEE Trans. Robot.*, vol. 38, no. 1, pp. 302–316, Feb. 2022.
- [62] M. J. Pollayil et al., "Choosing stiffness and damping for optimal impedance planning," *IEEE Trans. Robot.*, vol. 39, no. 2, pp. 1281–1300, Apr. 2023.

- [63] G. Gaspard et al., "Robust optimization of system compliance for physical interaction in uncertain scenarios," in *Proc. IEEE-RAS 16th Int. Conf. Humanoid Robots*, 2016, pp. 911–918.
- [64] R. Mengacci, F. Angelini, M. G. Catalano, G. Grioli, A. Bicchi, and M. Garabini, "Stiffness bounds for resilient and stable physical interaction of articulated soft robots," *IEEE Robot. Autom. Lett.*, vol. 4, no. 4, pp. 4131–4138, Oct. 2019.
- [65] T. Sugihara, *Historical Perspective and Scope*. Dordrecht, The Netherlands: Springer, 2019, pp. 665–674.
- [66] K. Bouyarmane et al., *Multi-Contact Motion Planning and Control*. Dordrecht, The Netherlands: Springer, 2019, pp. 1763–1804.
- [67] H. K. Khalil, *Nonlinear Control*. London, U.K.: Pearson, 2015.



Alok Ranjan (Student Member, IEEE) received the B.Tech. degree in mechanical engineering from the Krishna Institute of Engineering and Technology, Ghaziabad, India, in 2012, the M.Tech. degree in structures and design from the Indian Institute of Space Science and Technology, Thiruvananthapuram, India, in 2016, and the M.Sc. degree in biomedical engineering from the University of Groningen, Groningen, The Netherlands, in 2020. He is currently working toward the Ph.D. degree in robotics with the

University of Pisa, Pisa, Italy.

His main research interests include design and control of bioinspired and compliant mechanisms.



Franco Angelini (Member, IEEE) received the B.S. degree in computer engineering, the M.S. degree (*cum laude*) in automation and robotics engineering, and the Ph.D. degree (*cum laude*) in robotics from the University of Pisa, Pisa, Italy, in 2013, 2016, and 2020, respectively.

He is currently an Assistant Professor with the University of Pisa. His main research interests include control of soft robotic systems, impedance planning, and robotic environmental monitoring.



Thrishantha Nanayakkara (Senior Member, IEEE) received the B.Sc. degree from the University of Moratuwa (UM), Moratuwa, Sri Lanka, in 1996, and the M.Sc. degree from the Saga University (SU), Saga, Japan, in 1998, both in electrical engineering, and the Ph.D. degree in robotics from SU, in 2001.

He was a Postdoctoral Research Fellow with the Department of Biomedical Engineering, Johns Hopkins University, Baltimore, MD, USA, from 2001 to 2003, a Senior Lecturer with the Faculty of Engineering, UM, a Radcliffe Fellow with Harvard University, Cambridge, MA, USA, from 2008 to 2009, a Research Affiliate with MIT, Cambridge, MA, USA, from 2008 to 2009, and a Senior Lecturer with the Department of Informatics, King's College London, U.K., from 2012 to 2016. He is currently a Reader with the Dyson School of Design Engineering, Imperial College London. His research interests include soft robotics, and robotic interaction with uncertain environments.



Manolo Garabini (Member, IEEE) received the graduation degree in mechanical engineering and the Ph.D. degree in robotics from the University of Pisa, Pisa, Italy, in 2010 and 2014, respectively.

He is currently employed as Professor with the University of Pisa. Currently, he is the Principal Investigator with the THING H2020 EU Research Project for the University of Pisa, and the Coordinator of the Dysturbance H2020 Eurobench subproject. Finally, he is the Coordinator

of the H2020 EU Research Project Natural Intelligence. His main research interests include the design, planning, and control of soft adaptive robots.